Macromolecules
ARTICLE

Macromolecules **2009**, *42*, 8251–8259 **8251**
DOI: 10.1021/ma901419y

Long-Term Operations of Polymeric Thin-Film Transistors: Electric-Field-Induced Intrachain Order and Charge Transport Enhancements of Conjugated Poly(3-hexylthiophene)

Horng-Long Cheng,*,† Jr-Wei Lin,†,§ Ming-Feng Jang,†,§ Fu-Chiao Wu,† Wei-Yang Chou,† Ming-Hua Chang,† and Ching-Hsun Chao‡

†*Institute of Electro-Optical Science and Engineering, Center for Micro/Nano Science and Technology, Advanced Optoelectronic Technology Center, National Cheng Kung University, Tainan 701, Taiwan, R.O.C, and* ‡*Department of Materials Science and Engineering, MingDau University, Chang-Hwa 523, Taiwan, R.O.C.* §*J.-W. Lin and M.-F. Jang contributed equally to this work.*

Received July 1, 2009; Revised Manuscript Received October 9, 2009

ABSTRACT: This study focuses on the microstructural modifications of regioregular poly(3-hexylthiophene) (rr-P3HT) in the small active channel of thin-film transistors (TFTs) during operations. Polarized absorption and micro-Raman spectroscopy analyses allow us to probe directly the conformation transitions of rr-P3HT chains parallel or perpendicular to the channel by means of exciton bandwidth, interchain electronic coupling, and effective conjugation length. The results of absorption spectra and a joint experimental−theoretical study of Raman spectra show that an external source-to-drain electric field can align rr-P3HT chains parallel to the channel, improving electrical performance after long-term operations, especially charge transport properties. In comparison, the applied external gate field induced an increase in amorphous fraction of the rr-P3HT films. After the analysis, we propose a chain rearrangement model driven by an external electric field to interpret the changes of the effective conjugation length of rr-P3HT, rather than thermal annealing. Our observations provide a thorough explanation for the previously unknown relationships of structure−electronic properties under the extended operations of polymer TFT devices.

Introduction

Conjugated polymeric semiconductor-based thin-film devices have become a topic of great interest due to their potential applications for flexible, lightweight, scalable, and low-cost microelectronic and optoelectronic devices. A large number of polymeric semiconductors have now demonstrated performance (i.e., field-effect mobility above 0.1 $cm^2/(V\,s)$), which makes them applicable in thin-film transistor (TFTs) technologies.[1,2] In recent years, significant effort has been devoted to understanding the fundamental relationships between the electrical characteristics of TFTs and structural properties (from microscopic electronic structure to solid-state microstructure) of polymeric semiconductors.[1−12] To date, however, there is little known about the impact of the application of the external electric field and long-term operations on the above-mentioned structural properties of polymeric semiconductors and, thus, electrical properties and the stability of polymeric TFT devices.[1,3] With strict reliability and lifetime requirements, the organic/polymeric devices are progressing to commercial applications greatly. It is important to perceive the variation in the molecular properties and device characteristics from long-term operations.

During device operations, the application of the external electric field can have significant effects on charge transport behaviors and electrical characteristics of organic TFTs.[3] For disordered polymer semiconductors, the field dependence mobility generally obeys a Poole−Frenkel behavior, in which the charge mobility increases at high fields in the range of 10^4-10^6 V/cm.[1,3] From the viewpoint of molecular properties, the presence of an external electric field influences the wave function and leads to induced dipole, quadrupole, etc., moments, thus making the molecular orbitals no longer optimal in the vibrational sense.[13] Concerning the operational stability of polymeric devices,[1,14−20] many researchers have reported that bias-stress-induced instability (in general, threshold voltage (V_{th}) shift) leads to device degradation in terms of electrical characteristics and, thus, TFT performance. Therefore, it is generally accepted that the application of large electric fields alters the semiconductor properties of the organic materials due to the generation of defects and gap states and the trapping of charges.[21,22] These effects are more pronounced in the presence of moisture and/or oxygen than when the device is operated in a vacuum or in dry air.[1] On the contrary, several research groups have observed almost unchanged mobility of polymer-based TFTs after bias-stress and/or long-term operations.[14,15,17,20,23] However, the physical origins of such observations are not clear due to the complex microstructure of polymer films, which in many cases cannot be fully characterized by conventional diffraction and microscopy techniques. In our previous studies, in situ micro-Raman spectroscopy has been proven to directly probe the molecular properties of organic semiconductors, e.g., pentacene, within the small active channel of TFTs during operations.[24] Recently, we have found that applied external electric fields alter the molecular geometry and induce irreversible structural phase transitions of pentacene in a TFT's channel, explaining the improved electrical properties (especially charge transport properties) that develop under extended operation.[25] To the best of our knowledge, a systematic study involving the change in molecular properties and microstructure of conjugated polymers during long-term operations of TFTs is still missing. The aim of this paper is to report on such an

*To whom correspondence should be addressed: e-mail shlcheng@mail.ncku.edu.tw.

Published on Web 10/19/2009

investigation. For real applications, the stability and reliability of TFTs are important key factors to realizing more complex electronic and circuit applications. In particular, when the devices are scaled down to nanoscale dimensions, the increase of the electric field will have a profound impact on the above-mentioned issues.

In this study, we report experimental observations of chain conformation and microstructural modifications of regioregular poly(3-hexylthiophene) (rr-P3HT) in the active channel of TFTs after long-term operations by using polarized absorption and micro-Raman spectroscopy. For application in polymer TFT technologies, rr-P3HT attracts attention due to its great charge mobility (above 0.1 $cm^2/(V\ s)$).[1,4,6−8] After extended operations of rr-P3HT-based TFTs, we observed a surprising improvement of electrical performance. Polarized spectroscopy analyses allowed us to directly probe the conformation changes of rr-P3HT chains that are parallel (denoted as *X*-direction) or perpendicular (denoted as *Y*-direction) to the active channel of TFT. Absorption spectroscopy has provided a powerful tool for determining the exciton bandwidth (W), interchain electronic coupling (J), and thus the effective conjugation length (L_{eff}) of conjugated polymers.[10,12,26,27] Consequently, the L_{eff} of rr-P3HT chains in TFTs before and after extended operations can be compared. A joint experimental−theoretical study on the Raman spectra also provided a method for detecting the extension of the L_{eff} and the microstructural homogeneity of conjugated polymers. After the analysis, electric-field-induced intrachain order enhancements of rr-P3HT chains could be interpreted as performing well according to the analysis of absorption and Raman spectroscopy and our proposed structural model. Additionally, the impact of the source-to-drain electric field ($\vec{E}_{SD}$), gate electric field ($\vec{E}_G$), and thermal heating effects on structural changes of the rr-P3HT films during device operations were also examined.

Experimental Section

Sample Preparation. The TFT substrate with prefabricated indium−tin oxide (ITO) as the gate and source/drain electrodes and a conventional silicon dioxide (SiO_2) as gate dielectric used in the experiments have been described previously.[25] Before deposition of rr-P3HT films, the TFT substrate was treated with oxygen plasma (Drytek MS6 Plasma Etcher Mega Strip 6). Then, the TFT substrate was transferred into a glovebox under a nitrogen atmosphere, and the following procedures were carried out. The rr-P3HT (M_w of 87 000 g/mol, 98.5% regioregular, Aldrich) films with a typical thickness of 60−70 nm were spin-coated from a 0.3 wt % anhydrous *p*-xylene solution (spinning speed 2000 rpm and spinning time 30 s) and baked at 120 °C for 2 h. The obtained rr-P3HT film was referred to as the "initial film". For reference purposes only, the following rr-P3HT films (or TFT devices) were also made from different experimental conditions. For the annealing test, the initial films were further annealed at 150 °C for 24 h in a vacuum, and the film was referred to as the "annealed film". For the thick film-based TFTs, the rr-P3HT films with a thickness of ca. 200 nm were spin-coated from a 0.3 wt % anhydrous *p*-xylene solution (spinning speed 500 rpm and spinning time 30 s) and baked at 120 °C for 2 h and called a "thick film" (or "thick device"). The thicknesses of the polymer films were determined by an Alpha-step (Tencor Instruments, Alpha-step IQ).

Device Characterization. The electrical characteristics of TFTs were measured by a Keithley 4200-SCS semiconductor parameter analyzer in a dark glovebox under a nitrogen atmosphere. The TFT characteristics were measured in a cyclic procedure. We defined a "full scan" as the following measurement procedures: (1) the output characteristics [drain current (I_{DS})−drain voltage (V_{DS})] were first measured, in which V_{DS} went from 0 V scan to −80 V at a different gate voltage (V_{GS}),

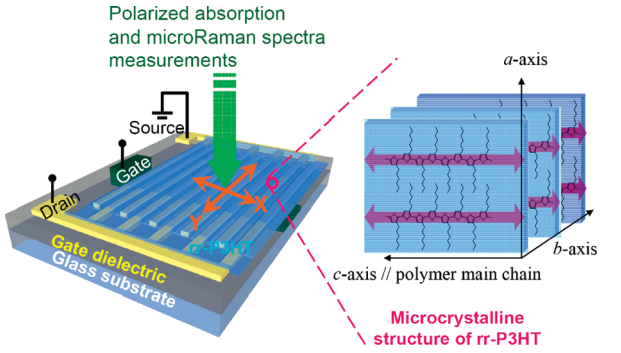

Figure 1. Schematic diagram of the TFT configuration used in this study and polarized spectra measurements setup. *X*- and *Y*-directions are defined as parallel and perpendicular to the active channel of TFT, respectively. Inset: self-assembled lamellar-like crystal orientations of rr-P3HT.

from 0 V to −80 V with a step of −10 V; (2) the transfer curves ($I_{DS}-V_{GS}$) were measured, in which V_{GS} from +40 V scan to −80 V at a different V_{DS} from 0 to −80 V with a step of −10 V. In the linear regime, the field-effect mobility (μ_{lin}) can be calculated from transconductance[1,28]

$$g_m = \left.\frac{\partial I_{DS}}{\partial V_{GS}}\right|_{V_{DS}=\text{const}} = \frac{WC_i}{L}\mu_{lin}V_{DS} \quad (1)$$

where C_i is the gate capacitance and W/L is the ratio of the channel width to channel length. In the saturation regime when $V_{DS} > V_{GS}$, the saturated field-effect mobility (μ_{sat}) can be calculated by fitting the following TFT model equation[1,28]

$$I_{DS} = \frac{WC_i}{2L}\mu_{sat}(V_{GS}-V_{th})^2 \quad (2)$$

Analytical Methods. The absorption spectra of rr-P3HT films were produced by a GBC Cintra 202 spectrometer with a scan rate of 1000 nm/min. The spectrophotometer resolution was below 0.9 nm. At least three absorption spectra were recorded on each sample. Micro-Raman spectra of rr-P3HT films, produced by lattice phonons, were obtained using a Jobin Yvon LabRam HR spectrometer. A 532 nm solid state laser and a 633 nm He−Ne laser served as the excitation light source and were kept below 0.5 mW to prevent thermal damage of the rr-P3HT film. The spatial resolution of the beam spot was around 1 μm, obtained using a 100× objective microscope lens. The spectrometer resolutions are within 0.4 and 0.2 cm^{-1} for 532 and 633 nm excitation lines, respectively. Every Raman spectrum was taken an average of 10 spectra, and at least three spectra were measured for each sample. Polarized Raman measurement is always perpendicular to the substrate, and the incident and detected light are always parallel to each other.

Quantum Chemical Calculations. The Gaussian 03 program[29] was used to perform the density functional theory (DFT) calculations. The geometry optimizations and vibrational frequency calculations of oligo(thiophene)s with thiophene units up to 14 were performed by using DFT at the B3LYP[30]/6-31G(d) level of theory. All geometry optimizations were performed using direct inversion in the iterative subspace (GDIIS) method with tight convergence criteria. The geometries are constrained to C_{2h} symmetry if n is even and C_{2v} symmetry if n is odd; thus, the planar conformation of the backbone can be ensured.

Results and Discussion

Electrical Properties. This study used a bottom-gate TFT structure with comb bottom-contact ITO source/drain

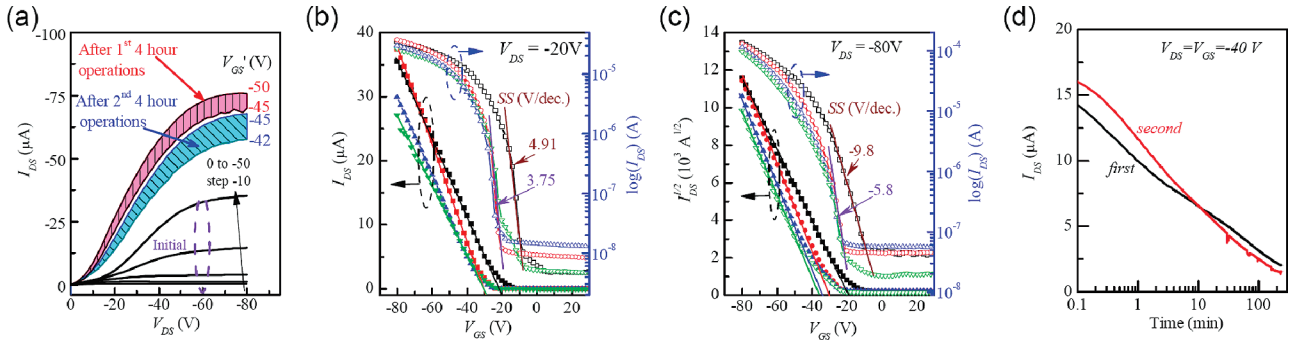

Figure 2. Typical electrical characteristics of rr-P3HT-based TFTs (L/W = 10 μm/20 mm) before and after long-term operations. (a) Output curves at the selected effective gate bias ($V_{GS}' = V_{GS} - V_{th}$). The thin lines indicate the device at the initial state. After long-term operations, the device then performed a "full scan" nine times for 9 h, and the curves within the fill area indicate the observed curves at selected V_{GS}'. (b) Linear and (c) saturated transfer curves, respectively. Symbols: (■) initial state, (●) after first time, and (▲) after second time of 4 h continuous operations, respectively, and (▼) after second round of continuous operations and then after nine full scans for 9 h. (d) Comparison of first-time and second-time output current curves as a function of time.

electrodes on a glass substrate as a testing device (Figure 1). Such a transparent TFT substrate provides convenience for measuring directly the spectroscopic properties of rr-P3HT films within the channel. Moreover, the ITO electrode-based devices were very durable and suitable for long-term continuous operations.[25] In addition, oxygen plasma treatment was carried out on the TFT substrate to reduce the surface trap states of SiO_2 and improve the wetting of the rr-P3HT solutions. Consequently, the impact of operations on the chain conformations and molecular properties of rr-P3HT can be seen after a long-term operation of polymer-based TFTs. The rr-P3HT active layer on the SiO_2 surface[31,32] consists of a [100] peak at 5.4° 2θ that confirms that polymer backbones self-organize into a lamellar supramolecular structure (Figure 1, right panel) with an interlamellar packing distance of 16.4 Å.[4]

The present rr-P3HT devices exhibited good electrical properties with μ_{sat} of ca. 5×10^{-3}–3×10^{-2} cm^2/(V s) and an on/off current ratio more than 10^3 in our testing channel dimensions. The field-effect mobility depended on the channel dimensions; therefore, the comparison of field-effect mobility should be done at the same channel dimensions. The electrical characteristics of the rr-P3HT devices obtained in this study were comparable with previous studies by other researchers also using *p*-xylene as a solvent.[5–8] First, rr-P3HT TFTs with L/W of 10/20 μm/mm were tested and performed long-term continuous operations. The initial typical output and transfer characteristics are shown in Figure 2. The device showed the μ_{sat} of 6.0×10^{-3} cm^2/(V s). Then, the device was operated continuously at $V_{GS} = V_{DS} = -40$ V for 4 h, and the I_{DS} as a function of time was recorded in Figure 2d. Such I_{DS} decay behavior in organic TFT devices has been explained by a gate-bias stress effect and charge trapping mechanisms.[14,15,18,20] After the operations, a "full scan" per hour measurement was performed on the same device. Then, there was a rest break of 1 h to reduce the effects from the transient trap state. After the first round of continuous operations, the device showed improved output (Figure 2a) and transfer electrical characteristics (Figure 2b,c) such as larger I_{DS}, higher mobility, and a sharper subthreshold swing (SS) behavior. Next, the device was operated nine times at "full scan" for 9 h; the corresponding output curves are shown in Figure 2a, and the μ_{sat} recorded is shown in Figure 3. After 10 h, the device was operated continuously at $V_{GS} = V_{DS} = -40$ V for another 4 h, and the I_{DS} as a function of time was recorded as a trace "second" (Figure 2d). After the operations, the device still showed higher I_{DS} curves (Figure 2a), improved mobility

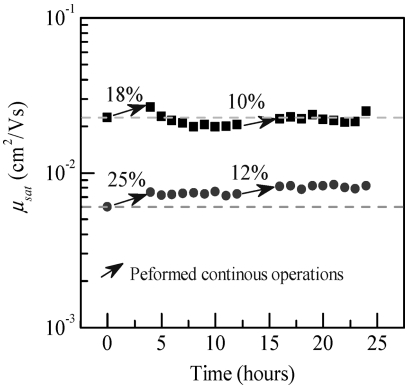

Figure 3. Recorded saturated field-effect mobilities (μ_{sat} at V_{DS} of −80 V) as a function of experimental time. The arrows indicate that the devices were performing 4 h of continuous operation at $V_{DS} = V_{GS} = -40$ V. The incremental amounts for μ_{sat} after continuous operation were also shown. The channel length of the devices: (■) 30 μm; (●) 10 μm. The devices have the same channel width of 20 mm.

(Figure 3), and sharper SS behavior (Figure 2b,c) than that of the initial state. After additional prolonged storage, the device continued to work properly.

Similar experiments of rr-P3HT TFTs with different channel lengths also were conducted, and as a result, we found analogous behavior. For comparison, the μ_{sat} recorded as a function of time for the device with L/W of 30/20 μm/mm is shown in Figure 3. Our experimental results show a high level of replication based on the use of many devices with various channel dimensions. Obviously, previous arguments do not provide a thorough explanation for the improved electrical characteristics of the present polymeric TFTs upon prolonged operation.[1,14–23] In some cases of polymeric TFTs, gate bias-stress-induced instability has been found to be reversible and having no significant degradation.[14,15,17,18] These results suggest that polymeric TFTs can exhibit device stability and reliability. Then, we used the polarized absorption and micro-Raman spectra to trace the polymer chain conformation changes within the channel, justifying the improved electrical properties.

Optical Absorption Properties. Figure 4 displays the polarized absorption spectra of rr-P3HT films within the active channel before and after long-term operations.[34] The rr-P3HT films show an absorption maximum (λ_{max}) at 556 nm (assigned as A_1 band). After long-term operations, striking differences were found in the spectra in the films in the *X*- and *Y*-directions, especially in a shoulder at 602 nm (assigned as

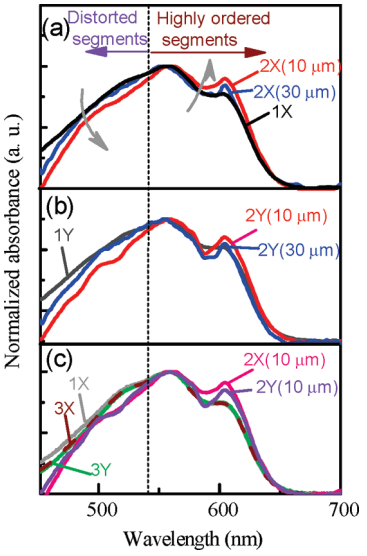

Figure 4. Polarized absorption spectra of the rr-P3HT films within different channel lengths of TFTs before (denoted by 1) and after (denoted by 2) long-term operations. (a) Parallel (denoted by *X*) and (b) perpendicular (denoted by *Y*) to the active channel of TFTs. (c) Comparison of the spectra of the initial films, annealed films (denoted by 3), and the operated films. The numbers in parentheses are the channel length of TFTs. The dashed lines serve as guidelines.

A_0 band) and the absorption in the wavelength lower than 540 nm. Previously, the A_0 band has been proven related to the long-range ordered structure; the intensity increases with a higher degree of crystallinity.[35,36] On the other hand, experimental results and theoretical predictions have suggested that the measured absorption for wavelengths lower than 540 nm is due to the chains with short L_{eff}, i.e., more distorted segments, from the amorphous region.[27] In long-term operations, the rr-P3HT in a 10 μm channel showed a λ_{max} at 560 nm, which is 4 nm red-shifted compared to the initial state; the A_0 band becomes stronger, but the relative intensities at a shorter wavelength (< 540 nm) are decreased when compared to those in the initial state in the *X*- and *Y*-directions. Consequently, we found that the amorphous portion of polymeric film can be transformed into a crystalline portion during device operations.

According to recent theoretical calculations based on an H-aggregate model,[10,26] the magnitude of the *W* of rr-P3HT can be estimated from the absorbance intensity ratio of the A_0 and A_1 bands by using the following expression

$$\frac{A_0}{A_1} \approx \left(\frac{1 - 0.24W/E_p}{1 + 0.073W/E_p} \right)^2 \qquad (3)$$

where E_p is the energy of the main intramolecular vibration coupled to the electronic transition. Using E_p of 0.18 eV (C=C stretching vibration in the thiophene ring)[10] and the experimental absorbance ratio shown in Figure 4, the estimated values of *W* are listed in Table 1. For the initial films, the average value of *W* was ~76 meV with a standard variation of 5 meV based on at least 10 specimens. Moreover, the initial rr-P3HT films displayed similar *W* values in the *X*- and *Y*-directions, suggesting an isotropic structural feature. However, after long-term operations, the rr-P3HT films displayed smaller *W*, especially in the *X*-direction. Quantum-chemical calculations have shown that increasing the L_{eff} of conjugated polymers reduces the *J*,[37] decreasing the value of *W* (*W* = 4*J* for free exciton bandwidth) when the

Table 1. Comparison of the Absorption Maximum (λ_{max}), Exciton Bandwidth (*W*), Interchain Electronic Coupling (*J*), and Relative Effective Conjugation Length (L_{eff}) of rr-P3HT in the Active Channel of TFTs before and after Long-Term Operations

channel length (μm)	operation conditions	measured direction[a]	λ_{max} (nm)	*W* (meV)	*J* (meV)	L_{eff}
10	before	*X*	556	73.2	18.3	1.00
		Y	556	74.3	18.6	0.99
	after	*X*	560	31.1	7.8	1.68
		Y	559	45.7	11.4	1.36
30	before	*X*	556	75.3	18.8	1.00
		Y	556	76.0	19.0	0.99
	after	*X*	557	48.0	12.0	1.28
		Y	556	63.3	15.8	1.10

[a] *X* and *Y* denoted as the directions that parallel and perpendicular to the active channel of TFTs, respectively.

L_{eff} is longer than the intermolecular separation. Therefore, it was expected that the L_{eff} in the initial films (with $W \sim 76$ meV) would be larger than 20−30 monomers according to recent theoretical predictions.[27,38] For example, Clark et al.[27] observed that the rr-P3HT film made from chloroform solution has a *W* value of ~120 meV. They suggested that a corresponding L_{eff} would have 20−30 monomers based on Zerner's intermediate neglect of differential overlap (ZINDO) method. Here, the present rr-P3HT film has a smaller *W* value than the chloroform film, suggesting a longer L_{eff}. Using Barford's model,[39] the relative L_{eff} could be estimated with scaling relations: $J \sim L_{eff}^{-1.8}$ for parallel conjugated chains, just as in the rr-P3HT case. We assumed that the L_{eff} of the initial film in the *X*-direction before operations equals unity, $L_{eff} = 1$ (one). The estimated relative L_{eff} values are listed in Table 1. In the *X*-direction the L_{eff} had a larger improvement than the *Y*-direction in both devices with *L* of 10 and 30 μm, indicating the anisotropic structural properties. By combining Spino's model and Barford's equation, it could mean that it is difficult to cause a further increase of the A_0 band intensity when L_{eff} is gradually extended (also see Supporting Information Figure S1). In other words, when the A_0/A_1 value is high (e.g., larger than 0.8), a slight increase of A_0/A_1 value implies the largely extended L_{eff}. Meanwhile, a considerable narrowing of the spectrum shape and a red shift of A_1 band suggest that the extent of the conjugation of rr-P3HT is more homogeneous.

It is well-known that TFT devices will undergo thermal self-heating when operated at high voltage and high current, especially on a thermally insulating substrate, e.g., glass substrate. Previous reports on Si-based TFTs found that the self-heating effect causes the unsaturated I_{DS} in the output curve and/or device performance degradation.[40] Chabinyc et al.[41] examined the self-heating effects on the electrical characteristics of polymer-based, i.e., regioregular poly[5,5′-bis(3-dodecyl-2-thienyl)-2,2′-bithiophene], TFTs. They suggested that the self-heating cannot completely explain the rise in I_{DS} at high V_{DS} for polymer-based TFTs with a short channel. In Figure 2a, the output curves of the present rr-P3HT TFTs do not show a considerable unsaturated phenomenon even after long-term operations. Therefore, we conclude that the self-heating effect does not have a serious impact on the electrical characteristics of the rr-P3HT-based TFTs. However, the thermal energy generated from long-term operations of TFTs may provide a possible method of inducing structural changes of rr-P3HT films. Therefore, we conducted complementary annealing experiments (150 °C for more than 24 h) for the initial rr-P3HT film. The absorption spectra are shown in Figure 4c; the increment of L_{eff} was smaller than 10% in the *X*- and

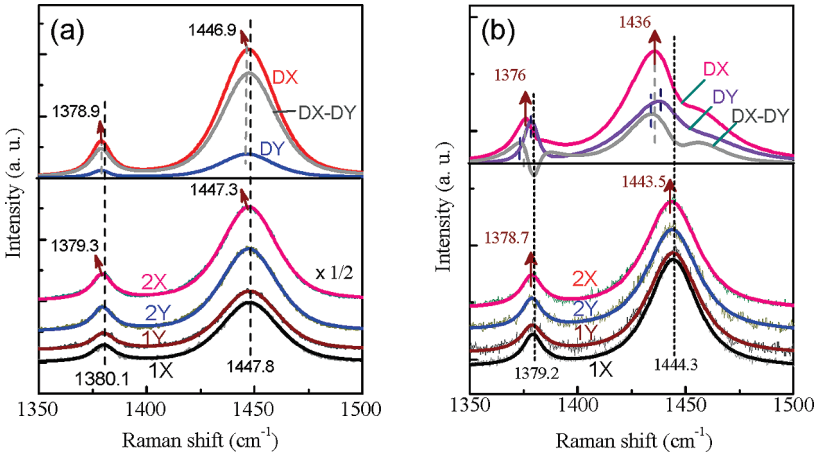

Figure 5. Comparison of polarized micro-Raman spectra of the rr-P3HT films within the active channel of TFTs (L/W = 10 μm/20 mm) before (denoted by 1) and after (denoted by 2) long-term operations: (a) λ_{exc} = 532 nm; (b) λ_{exc} = 633 nm. The *X*- and *Y*-directions are parallel and perpendicular to the channel, respectively. The solid curves represent the best fit with a Gaussian/Lorentzian function, while the thin lines to the experimental data. Traces DX and DY are obtained by subtracting 1X from 2X and 1Y from 2Y, respectively. Trace DX−DY is obtained by subtracting the DY from DX. The dashed lines serve as guidelines. [Note: the best-fit spectra were used to obtain the difference spectra.]

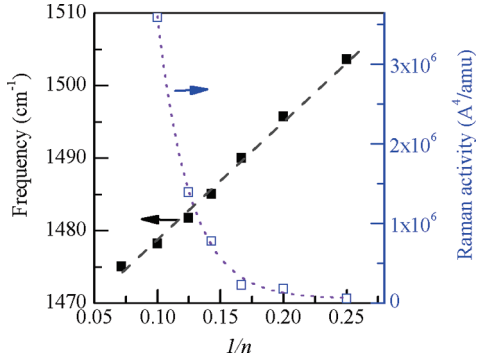

Figure 6. DFT calculated frequencies (left axes) and Raman activity (right axes) of the strongest symmetric $C_\alpha-C_\beta$ stretching (ν_1) band versus the reciprocal of the number of thiophene units ($1/n$) for oligo(thiophene)s. The dashed and dotted lines are fitted to a linear and an exponential decay law, respectively.

Y-directions. The initial films were annealed at 120 °C for 2 h before running any test, making the films very stable and reliable. Obviously, simply thermal effects would not allow the rr-P3HT chains to reorganize and therefore increased L_{eff} significantly and led to anisotropic structural changes of the initial films. In summary, we believe that the electric field applied during device operations may dominate the increases in L_{eff} of rr-P3HT films.

Raman Spectroscopy. The increased L_{eff} is confirmed by joint polarized micro-Raman spectroscopic measurements (Figure 5) and DFT vibrational analysis (Figure 6). We focused on the vibrational modes coupled to the electronic transition at the region of 1350−1500 cm^{-1}, that is, the most intense symmetric $C_\alpha-C_\beta$ stretching deformation (~1448 cm^{-1}, denoted as ν_1 band) and $C_\beta-C_\beta$ stretching deformations (ca. 1380 cm^{-1}, denoted as ν_2 band) exist in the aromatic thiophene ring.[42]

The Raman spectra of the initial film in the *X*- and *Y*-directions showed the same spectrum shape, e.g., similar center frequency and half-width (β) of the ν_1 and ν_2 bands, even using different laser sources (532 and 633 nm), as shown in Figure 5. However, the peak center frequency of the ν_1 and ν_2 bands depends on the excitation energy. When we used a 532 nm excitation line with the wavelength located at the disorder/order (amorphous/crystalline) crossover regime, the peak centers of the ν_1 and ν_2 bands are located at 1447.8 and 1380.1 cm^{-1}, respectively. In contrast, the peak centers downshift to ca. 1444.3 and 1379.2 cm^{-1} by 3.5 and 0.9 cm^{-1}, respectively, for the ν_1 and ν_2 bands when using a 633 nm laser. A 633 nm laser with energy was located at the red edge of absorption; therefore, an enhancement of the Raman band feature related to the ordered structures was observed. The downshift of Raman lines can be interpreted with a theoretical vibrational analysis of oligo(thiophene)s (*n*T) with a different number of thiophene rings (n). Figure 6 shows a good linear curve of the frequency of the ν_1 band against the reciprocal of the n. Therefore, the ν_1 band downshifts by 3.5 cm^{-1}, indicating the greater contribution of long conjugation segment vibrations in the film. The results are consistent with early studies on aromatic ring vibrations in the π-conjugated polymer systems, e.g., poly(*p*-phenylene vinlylene)[43] and polythiophenes,[42] where the increasing L_{eff} causes the Raman lines to downshift. Consequently, the 532 and 633 nm excitation lines allow us to obtain the structural information related to the chains in the disordered (amorphous) and highly ordered (crystalline) regions, respectively. (Note: when using a 633 nm excitation line, the relative weak Raman signals, i.e., slightly enlarged noise, of the films were due to low resonance with electronic transitions and low laser power which aim to minimum thermal damage to rr-P3HT films.)

The results of long-term operations on the *X*- and *Y*-directions of the Raman spectra from the rr-P3HT films are shown in Figure 5. Using a 532 nm laser (see Figure 5a), we observe a slight downshift of the ν_1 and ν_2 bands by 0.4 and 0.8 cm^{-1} in the *X*-direction (by 0.3 and 0.4 cm^{-1} in the *Y*-direction), respectively, compared to the initial film. For the initial rr-P3HT films, it is hard to cause a downshift of the Raman bands (the standard derivations are smaller than 0.1 cm^{-1}).[44] The results suggested that the initial films have stable structural properties with fine L_{eff}. Even after a postannealing for more than 24 h at 150 °C to improve the structural quality, the resulting downshifts of the ν_1 band were only 0.2 cm^{-1} in the *X*- and *Y*-directions (see Supporting Information Figure S2). Quantum-chemical calculations (Figure 6, left axes) show that it becomes more difficult to observe the frequency shift of the Raman line with the increasing of L_{eff}. In addition, we also observed an enhanced Raman intensity of the films after long-term operations,

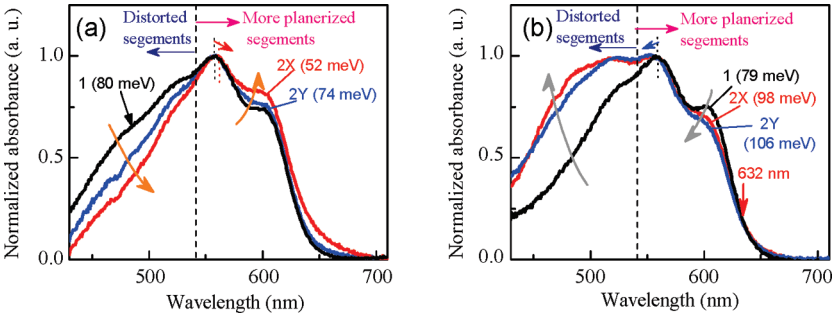

Figure 7. Comparison of absorption spectra of the rr-P3HT films in the channel of TFTs before (trace 1) and after (trace 2) the operations of applying the (a) drain bias ($V_{DS} = -60$ V for 10^3 s) and (b) gate bias ($V_{GS} = -40$ V for 10^4 s). *X* and *Y* are the directions parallel and perpendicular to the active channel, respectively. The numbers in parentheses are the calculated values of the exciton bandwidth. The dashed lines serve as guidelines.

especially in the *X*-direction. According to Figure 6 (right axes), the increase of *n*, i.e., L_{eff}, results in a rapid increase of Raman activity of the ν_1 band. Consequently, the increased intensity (or integrated peak area) suggests an enhanced L_{eff} of rr-P3HT films in the *X*-direction more than the *Y*-direction, confirming the anisotropic structural properties (also see the subtraction spectra in Figure 5a).[44] Furthermore, using a 532 nm laser, we observed more reduction of β of the Raman bands in the *X*-direction (30.9 and 11.9 cm^{-1} for ν_1 and ν_2 bands, respectively) than in the *Y*-direction (31.5 and 12.0 cm^{-1} for ν_1 and ν_2 bands, respectively) of the operated film compared to the initial films (32.1 and 13.3 cm^{-1}, for ν_1 and ν_2 bands, respectively).[44] After long-term operations, the reduced β of the Raman bands indicates more structural/environmental homogeneity and better interchain order in the disordered region. Considering the charge transport at the microscopic level,[3] the reduced β in absorption and resonance Raman spectra also suggest a lower vibrational reorganization energy that benefits the charge transfer.[45]

Next, we used a 633 nm excitation line to explore the evolution of highly ordered structure in the films after long-term operations (see Figure 5b). First, we observe an enlarged downshift of the ν_1 bands by 0.8 cm^{-1} in the *X*-direction after long-term operations when compared to the 532 nm excited spectra (only 0.4 cm^{-1}). In the *Y*-direction, however, the downshift of the ν_1 bands was only 0.3 cm^{-1}. When watching the difference spectra in Figure 5b (upper panel), a relatively low frequency peak of the ν_1 band at ca. 1436 and 1438 cm^{-1} (ν_2 band at ca. 1376 and 1378 cm^{-1}) was observed in the *X*- and *Y*-directions. As in Figure 5a (upper panel), we observe an increased intensity in the *X*-direction. This observation provided strong evidence that the structural qualities in the *X*-direction are superior to those in the *Y*-direction after long-term operations (also see the trace DX−DY in the upper panel of Figure 5b). Furthermore, the above-mentioned observations were also supported by the difference spectra, which obtained by subtracting the normalized spectra (intensity of strongest peak normalized to 1.0) of the operated film from the initial film (see Supporting Information Figure S3). In comparison, no clear anisotropic signal in Raman spectroscopy was detected for the initial and annealed films (see Supporting Information Figure S2).

Electric Field Effects. The effects of $\vec{E}_{SD}$ and $\vec{E}_G$ on rr-P3HT structural changes in TFT devices were examined by applying drain bias or gate bias for a period of time. The results of absorption spectra of the rr-P3HT films are shown in Figure 7. In this figure, the changes of the corresponding spectra are easily observed, even when only applying the $\vec{E}_{SD}$ (Figure 7a) or $\vec{E}_G$ (Figure 7b). When only applying the $\vec{E}_{SD}$, the observed changes in the absorption spectra are very similar to the data observed after long-term operations. The results are summarized as follows: (1) the intensity of the A_0 band increased, (2) the absorption peak maximum (A_{max}) and the onset of absorption onset show red shifts, and (3) there was a significant decreased absorbance in wavelengths lower than 540 nm. In the *X*-direction, we observe a more pronounced behavior than in the *Y*-direction. Taking the *W* value (shown in Figure 7a) and assuming L_{eff} of the initial film was one, the calculated L_{eff} was 2.17 and 1.15 in the *X*- and *Y*-directions, respectively. We observed a large increment of L_{eff} in the direction parallel to the $\vec{E}_{SD}$ field as compared to that of the device operating in the saturation regime for a long time (see Table 1). The results indicates that the $\vec{E}_{SD}$ field dominates the increase in L_{eff} and produces anisotropic structural properties of rr-P3HT films.

On the contrary, only applying the $\vec{E}_G$ to the rr-P3HT film, the absorption spectra exhibit an opposite tendency (Figure 7b); the intensity of the A_0 band decreased, there was a considerable increase in absorbance in wavelengths lower than 540 nm, and a blue shift of A_{max} in the *X*- and *Y*-directions. The results suggested that the $\vec{E}_G$ field will reduce the extent of conjugation and the L_{eff} of chains and then increase the disorder/amorphous portion in the films. In Figure 7b, we observe a reduction in L_{eff} after the operations by a factor of approximately 30−40%. After repeating the experiment many times, we could not see clear anisotropic structural properties induced by the $\vec{E}_G$ field. Such $\vec{E}_G$-driven structural changes of rr-P3HT films in the active channel could be verified further with Raman spectroscopic studies, as shown in Figure 8. Here we used a 633 nm excitation line to monitor the structural variations of the films, particular in the highly ordered/crystalline region. After applying the $\vec{E}_G$ field for a while, the rr-P3HT films show a significant decrease in Raman intensity (also see trace DX and DY in Figure 8), and the ν_1 and ν_0 bands are shifted slightly to a higher frequency by approximately 0.4−0.7 cm^{-1} in the *X*- and *Y*-directions. From the subtraction spectra in Figure 8 (trace NDX), we observe that the relative intensity of the low-frequency part (peak center at ca. 1432 cm^{-1}) was reduced, while the higher frequency part (peak center at ca. 1449 cm^{-1}) was increased. This result also demonstrates that the $\vec{E}_G$ field would create structural defects in the chains, reducing the L_{eff} as observed by optical absorption spectroscopy.

Structural Model. Figure 9 proposes a simple vector model with electric field−dipole moment interaction to rationalize the structural modifications of rr-P3HT films in the channel of TFT devices during operations. Here, we assume that the initial rr-P3HT chain has an intrinsic dipole moment P_0 vector in the Cartesian coordinates and the dipole is along the rr-P3HT backbones due to C−S−C polar bond in the

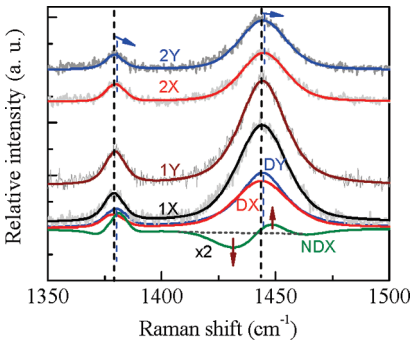

Figure 8. Polarized micro-Raman spectra (λ_{exc} = 633 nm) of rr-P3HT films in the channel of TFTs before (trace 1) and after (trace 2) the operations of only applying the gate bias (V_{GS} = −40 V for 10^4 s).The *X*- and *Y*-directions are parallel and perpendicular to the channel, respectively. The solid curves represent the best fit with the Gaussian/Lorentzian functions, while the thin lines correspond to the experimental data. Traces DX and DY are obtained by subtracting 2X from 1X and 2Y from 1Y, respectively. Trace (NDX) is obtained by subtracting the normalized spectrum of 1X from the normalized spectrum of 2X. The dashed lines serve as guidelines. [Note: the best-fit spectra were used to obtain the difference spectra.]

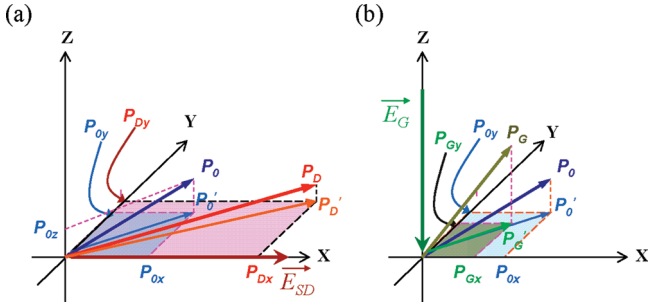

Figure 9. A simple vector model with electric field−dipole moment interactions: (a) drain field ($\vec{E}_{SD}$) and (b) gate field ($\vec{E}_G$) effects.

thiophene ring. The vector P_0' is the vector projection of P_0 on $X-Y$ plane. From spectroscopic data, the rr-P3HT chains have a random arrangement within the active channel of TFT, leading to a homogeneous isotropic film. The magnitude of the *X*-component (P_{0x}) and *Y*-component (P_{0y}) of P_0' vector is nearly equivalent in the initial film (also see definitions in Figure 9).

First, an $\vec{E}_{SD}$ field was applied along the *X*-axis direction. The interaction (*U*) between an electric field and the polymer was expressed as[46]

$$U = -\vec{E}\sum_j P_j \cos\theta_j \qquad (4)$$

where P_j is the dipole moment of the *j*th bond and θ_j is the angle between of the direction of the P_j and the field direction. There is a tendency for the molecules to align themselves with their dipole axes in the direction along the applied field; therefore, induced orientation polarization is produced. Equation 4 indicates that polarization of a polymer in an field occurs by chain subunits tending to align their dipolar and highly polarizable bonds with the field direction. In addition to the P_0, the extra dipole moment can be induced by the field and the charge motion along the polymer chain (i.e., current passing the polymer chain) can induce a dipole moment. The *U* should be large and have the capability to push the distorted segments into more planarized conjugation segments, and therefore, the resulting dipole moment P_D (and P_D') would be larger than the P_0 (and P_0') (note: P_D' as the vector projection of P_D on $x-y$ plane; see Figure 9a). DFT calculations of dipole moment of oligo(thiophene)s also support the observations in which the P_0 increased with the increasing *n*, e.g., P_0 = 0.41, 0.81, and 1.40 D for *n* = 4, 8, and 14, respectively. A dipole should align itself with an field and lead P_D toward the *X*-axis. The magnitude of *X*-component (P_{Dx}) is larger than the *Y*-component (P_{Dy}). Meanwhile, the P_{Dx} and P_{Dy} are both larger than the P_{0x} and P_{0y}, as illustrated in Figure 9a. The model provides a reasonable explanation for increased L_{eff} in the *X*- and *Y*-directions. Additionally, thermal self-heating from TFT's operations can cause the self-organization of polymer chains and lead to a slight increase of L_{eff} in the *X*- and *Y*-directions (also see Figure 4c). The self-heating effect may be one way to cause the increased L_{eff} in the *Y*-direction. Unfortunately, the effects of electric field and self-heating on structural changes of the rr-P3HT films could not be separated clearly during TFT's operations. However, we believe that the self-heating will increase the degree of polymer chain vibration due to increased input of thermal energy, thus speeding up rearrangement of the polymer chains under the field. Supporting this, Sugita and Tasaka[47] have shown that polymer chain conformation changed from a randomly coiled state to an oriented state due to the field−dipole interaction in the melt state. Kakade et al.[48] recently reported that an electric field used to macroscopically align polymer nanofibers can also align polymer chains parallel to the fiber axis.

On the basis of the proposed model, the $\vec{E}_{SD}$ effects are much more pronounced when the device has a smaller channel and/or is operated in the high field (i.e., saturation regime). Such electric-field-induced conformational changes in rr-P3HT are irreversible processes, and the induced dipole moment of a polymer in an electric field is proportional to the strength of the field. The $\vec{E}_{SD}$ strength in the 10 μm channel is 3 times that of the 30 μm channel; we also observed a similar amount of L_{eff} (also see Table 1).

Next, we consider the effect of the $\vec{E}_G$ field on structural changes of rr-P3HT films as illustrated in Figure 9b. The direction of the $\vec{E}_G$ field was assumed to be along the *Z*-axes. After the interaction between $\vec{E}_G$ and P_0, the resulted dipole P_G would be toward the *Z*-axes and therefore lead to the reduced magnitude of vector projection of P_G on $x-y$ plane (P_G'). The magnitude of the *X*-component (P_{Gx}) and *Y*-component (P_{Gy}) of P_G' both are smaller than that of P_{0x} and P_{0y}. Under ideal conditions, if the charge distribution induced by $\vec{E}_G$ was uniform within the channel, P_{Gx} and P_{Gy} should be approximately equal. On the other hand, if any nonuniformity takes place in the charge distribution of the active layer, this may induce a field along a specific direction; therefore, P_{Gx} and P_{Gy} would be unequal. Consequently, we observe a slight difference between the two spectra in the *X*- and *Y*-directions (Figure 7b). From the viewpoint of chain conformation, the reduced dipole moment suggests a short L_{eff} and an increase in the distorted segments (or defect) in the conjugation chains. Therefore, we saw an increased disorder/amorphous fraction in the film as evidenced by the absorption and Raman spectroscopic measurements.

When the rr-P3HT TFTs were operated in the saturation regime (e.g., V_{DS} = V_{GS} = −40 V), the magnitude of $\vec{E}_{SD}$ (e.g., 40 kV/cm when *L* = 10 μm) is relatively weaker than that of the $\vec{E}_G$ (e.g., >1 MV/cm if the thickness of rr-P3HT is ~70 nm). However, after long-term operations, we still observe a structural improvement of the rr-P3HT films. Besides electric field, according to eq 4, the *U* also depends on the p_j and the angle θ_j. On the rr-P3HT films

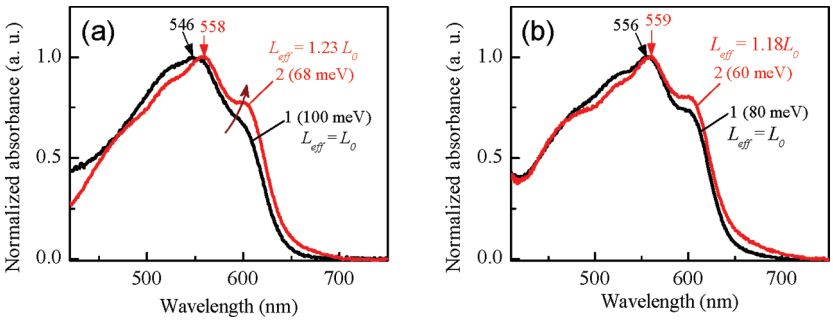

Figure 10. Comparison of absorption spectra of the (a) thick and (b) thin rr-P3HT films parallel to the channel of TFTs before (trace 1) and after (trace 2) the operations of applying the $V_{DS} = V_{GS} = -40$ V for 6×10^3 s. The numbers in parentheses are the calculated values of the exciton bandwidth. The relative effective conjugation length (L_{eff}) is also shown.

grown on SiO_2, we observed a [100] peak at ~5.37° 2θ (also see Figure 1),[31,32] suggesting there would be more large dipole moment components in the $X-Y$ plane than along the Z-axis (P_{0z}, also see Figure 9a) and the angle θ_j between the $\vec{E}_G$ and P_j would be larger than 45° (and even near 90°). Furthermore, the charge transport direction in a TFT device is parallel to the $\vec{E}_{SD}$, thus inducing a large dipole moment along the $\vec{E}_{SD}$. This may be why the $\vec{E}_{SD}$ dominates the structural changes of rr-P3HT films rather than the $\vec{E}_G$ field.

The impact of $\vec{E}_{SD}$ and $\vec{E}_G$ fields on the structural changes can be checked further using the rr-P3HT active layer with different thicknesses. For the thick film in the initial state, the absorption spectrum (Figure 10a) showed a blue shift of A_{max} and a reduced relative intensity of A_0 band compared to the thin film (Figure 10b) and therefore a larger value of W. The results suggest the inferior structural properties with short L_{eff} for the thick film. The observations are similar to that done by Joshi et al.[11] After long-term operations, we observed a more pronounced structural improvement of the thick device compared to a thin device. The phenomena now can be attributed to the $\vec{E}_G$ effect, which gradually decreases as the polymer thickness increases. Therefore, polymer films with lower thicknesses would have a large $\vec{E}_G$ effect, diminishing the effect from the $\vec{E}_{SD}$ field.

Discussion. Recently, several studies have suggested that the intrachain order of polymer chains, i.e., the L_{eff}, dominates the mobility in rr-P3HT-based TFT devices rather than in-plane π-stacking in some cases.[7,8,10] More recently, Grigorian and coauthors[48] have shown that the reduced $\pi-\pi$ distance in rr-P3HT films (characterized by in-plane grazing incidence X-ray scattering) does not lead to an increase of mobility. Clark et al. reported an excellent correlation between W obtained from the absorbance spectra and the mobility, obtained from TFTs.[12] Recently, we also have observed that the larger the A_0/A_1 absorbance ratio, the higher the mobility in rr-P3HT TFTs made using various solvents, including chloroform, toluene, *p*-xylene, and TCB.[31] In order to assess the negative effects from long-term bias stress on the device's characteristics, we used the TCB[6,12] as a solvent to prepare rr-P3HT active film with a W value of ca. 55 meV (note: slightly larger than that of the *p*-xylene device after extended operations). A comparison of absorption spectra of rr-P3HT films made from *p*-xylene (after long-term operations) and TCB (before device operation) also are provided in the Supporting Information Figure S4. After long-term operations, the *p*-xylene film shows a slight larger A_1 intensity and narrower spectrum width than the initial film spun from TCB, suggesting improved microstructure modified by the electric field. The μ_{sat} of the fresh TCB device (without any previous operations) measured with L/W of 10/20 μm/mm was μ_{sat} of 1.30×10^{-2} cm^2/(V s), which was larger than that of the *p*-xylene device after long-term operations ($\mu_{sat} = 8.1 \times 10^{-3} \pm 2 \times 10^{-4}$ cm^2/(V s)). The results imply that this may be due to the generation of negative effects of long-term bias stress such as electronic defect/trap states and mobility degradation, as previously suggested by other researchers.[1,19,21] The present study shows that the improved electrical properties of polymer-based TFTs after long-term operations are due to $\vec{E}_{SD}$-induced structural improvements of the rr-P3HT active layer, while for the $\vec{E}_G$ effect the disordered segments/amorphous fraction is increased significantly and therefore is unfavorable for charge transport. Consequently, we suggest that the $\vec{E}_G$-induced structural disorder in polymer films may provide an origin for the gate-bias stress-induced instability of polymer-based TFTs. In this study, we focus on the rr-P3HT films made from *p*-xylene solution. The same observations are true for rr-P3HT films made from other solutions, e.g., TCB and chloroform (see Supporting Information Figures S5 and S6).

Conclusion

We have demonstrated that the intrachain order of rr-P3HT chains can be enhanced by applying an electric field during the operations of polymeric TFTs, especially with polymer backbones parallel to the $\vec{E}_{SD}$. The results of the analyses of the polarized absorption and micro-Raman spectra indicated that the disordered chains reorganize into extended chains with improved homogeneity that are driven by $\vec{E}_{SD}$. The microstructural improvements observed in this study could provide a reasonable explanation for increased charge mobility after long-term operations. Using the electric field−dipole interaction model, we can explain the evolution of the conformation of the polymer chains under the $\vec{E}_{SD}$ and $\vec{E}_G$ fields. The $\vec{E}_{SD}$ induced the polymer chain orientation in the direction along the active channel and produced anisotropic structural properties of the polymer active layer; therefore, it would be better for charge transport in TFT devices. In comparison, the large $\vec{E}_G$ field makes the planarized and ordered chains more distorted and increases the amorphous fraction in the films. This gives new insight into the gate-bias stress-induced instability of polymer-based TFTs from the viewpoint of structural properties of polymer active layer. Additionally, the effects of electric-field-induced intrachain order enhancements were larger than those induced by the thermal annealing process. Consequently, the concept of electric-field-induced orientation can provide an efficient approach to align polymeric chains with high degree of orientation and therefore anisotropic structural properties.

Acknowledgment. This work was supported by the National Science Council, Taiwan, through Grant NSC97-2221-E-006-245.

We are grateful to the National Center for High-Performance Computing of Taiwan for computer time and facilities.

Supporting Information Available: Theoretical prediction of the relationship between relative A_0/A_1 intensity and L_{eff}, Raman studies of the annealed films and anisotropic properties of the operated films, comparison of absorption spectra of the rr-P3HT films made from *p*-xylene and TCB solutions before and after long-term operations, and absorption spectroscopy studies of the rr-P3HT films made from TCB and chloroform solutions after long-term operations of TFTs. This material is available free of charge via the Internet at http://pubs.acs.org.

References and Notes

(1) Sirringhaus, H. In *Organic Field-Effect Transistors*; Bao, Z., Locklin, J., Eds.; CRC Press: Boca Raton, FL, 2007; Chapter 2.3. For device degradation mechanisms, please see pp 127−130.
(2) Facchetti, A. *Mater. Today* **2007**, *10*, 28–37.
(3) Coropceanu, V.; Cornil, J.; da Silva Filho, D. A.; Olivier, Y.; Silbey, R.; Brédas, J.-L. *Chem. Rev.* **2007**, *107*, 926–952.
(4) Sirringhaus, H.; Brown, P. J.; Friend, R. H.; Nielsen, M. M.; Bechgaard, K.; Langeveld-Voss, B. M. W.; Spiering, A. J. H.; Janssen, R. A. J.; Meijer, E. W.; Herwig, P.; de Leeuw, D. M. *Nature* **1999**, *401*, 685–688.
(5) Bao, Z.; Dodabalapur, A.; Lovinger, A. J. *Appl. Phys. Lett.* **1996**, *69*, 4108–4110.
(6) Chang, J. F.; Sun, B.; Breiby, D. W.; Nielsen, M. M.; Solling, T. I.; Giles, M.; McCulloch, I.; Sirringhaus, H. *Chem. Mater.* **2004**, *16*, 4772–4776.
(7) Kline, R. J.; McGehee, M. D.; Kadnikova, E. N.; Liu, J. S.; Frechet, J. M. J.; Toney, M. F. *Macromolecules* **2005**, *38*, 3312–3319.
(8) Surin, M.; Leclere, P.; Lazzaroni, R.; Yuen, J. D.; Wang, G.; Moses, D.; Heeger, A. J.; Cho, S.; Lee, K. *J. Appl. Phys.* **2006**, *100*, 0033712.
(9) Zen, A.; Saphiannikova, M.; Neher, I. D.; Grenzer, J.; Grigorian, S.; Pietsch, U.; Asawapirom, U.; Janietz, S.; Scherf, U.; Lieberwirth, I.; Wegner, G. *Macromolecules* **2006**, *39*, 2162–2171.
(10) Chang, F. C.; Clark, J.; Zhao, N.; Sirringhaus, H.; Breiby, D. W.; Anderasen, J. W.; Nielsen, M. M.; Giles, M.; Heeney, M.; McCulloch, I. *Phys. Rev. B* **2006**, *74*, 115318.
(11) Joshi, S.; Grigorian, S.; Pietsch, U.; Pingel, P.; Zen, A.; Neher, D.; Scherf, U. *Macromolecules* **2008**, *41*, 6800–6808.
(12) Clark, J.; Chang, F. C.; Spano, F. C.; Friend, R. H.; Silva, C. *Appl. Phys. Lett.* **2009**, *94*, 163306.
(13) Jensen, F. In *Introduction to Computational Chemistry*, 2nd ed.; Wiley-VCH: Weinheim, Germany, 2007; Chapter 10.
(14) Brwon, A. R.; Jarrett, C. P.; de Leeuw, D. M.; Matters, M. *Synth. Met.* **1997**, *88*, 37–55.
(15) Matters, M.; de Leeuw, D. M.; Herwig, P. T.; Brwon, A. R. *Synth. Met.* **1999**, *102*, 998–999.
(16) Rep, D. B. A.; Morpurgo, A. F.; Sloof, W. G.; Klapwijk, T. M. *J. Appl. Phys.* **2003**, *93*, 2082–2090.
(17) Salleo, A.; Endicott, F.; Street, R. A. *Appl. Phys. Lett.* **2005**, *86*, 263505.
(18) Street, R. A.; Chabinyc, M. L.; Endicott, F.; Ong, B. *J. Appl. Phys.* **2006**, *100*, 114518.
(19) Umeda, T.; Tokito, S.; Kumaki, D. *J. Appl. Phys.* **2007**, *101*, 054517.
(20) Mathijssen, S. G. J.; Cölle, M.; Gomes, H.; Smits, E. C. P.; De Boer, B.; McCulloch, I.; Bobbert, P. A.; De Leeuw, D. M. *Adv. Mater.* **2007**, *19*, 2785–2789.
(21) Lang, D. V.; Chi, X.; Siegrist, T.; Sergent, A. M.; Ramirez, A. P. *Phys. Rev. Lett.* **2004**, *93*, 076601.
(22) Knipp, D.; Northrup, J. E. *Adv. Mater.* **2009**, *21*, 2511–2515.
(23) Ficker, J.; Ullmann, A.; Fix, W.; Rost, H.; Clemens, W. *J. Appl. Phys.* **2003**, *94*, 2638–2641.
(24) Cheng, H. L.; Chou, W. Y.; Kuo, C. W.; Tang, F. C.; Wang, Y. W. *Appl. Phys. Lett.* **2006**, *88*, 161918.
(25) Cheng, H. L.; Chou, W. Y.; Kuo, C. W.; Wang, Y. W.; Mai, Y. S.; Tang, F. C.; Chu, S. W. *Adv. Funct. Mater.* **2008**, *18*, 285–293.
(26) Spano, F. C. *J. Chem. Phys.* **2005**, *122*, 234701.
(27) Clark, J.; Silva, C.; Friend, R. H.; Spano, F. C. *Phys. Rev. Lett.* **2007**, *98*, 206406.
(28) Sze, S. M. *Physics of Semiconductor Devices*; Wiley-Interscience: New York, 1981.
(29) Frisch, M. J.; Trucks, G. W.; Schlegel, H. B.; Scuseria, G. E.; Robb, M. A.; Cheeseman, J. R.; Montgomery, J. A., Jr.; Vreven, T.; Kudin, K. N.; Burant, J. C.; Millam, J. M.; Iyengar, S. S.; Tomasi, J.; Barone, V.; Mennucci, B.; Cossi, M.; Scalmani, G.; Rega, N.; Petersson, G. A.; Nakatsuji, H.; Hada, M.; Ehara, M.; Toyota, K.; Fukuda, R.; Hasegawa, J.; Ishida, M.; Nakajima, T.; Honda, Y.; Kitao, O.; Nakai, H.; Klene, M.; Li, X.; Knox, J. E.; Hratchian, H. P.; Cross, J. P.; Bakken, V.; Adamo, C.; Jaramillo, J.; Gomperts, R.; Stratmann, R. E.; Yazyev, O.; Austin, A. J.; Cammi, R.; Pomelli, C.; Ochterski, J. W.; Ayala, P. Y.; Morokuma, K.; Voth, G. A.; Salvador, P.; Dannenberg, J. J.; Zakrzewski, V. G.; Dapprich, S.; Daniels, A. D.; Strain, M. C.; Farkas, O.; Malick, D. K.; Rabuck, A. D.; Raghavachari, K.; Foresman, J. B.; Ortiz, J. V.; Cui, Q.; Baboul, A. G.; Clifford, S.; Cioslowski, J.; Stefanov, B. B.; Liu, G.; Liashenko, A.; Piskorz, P.; Komaromi, I.; Martin, R. L.; Fox, D. J.; Keith, T.; Al-Laham, M. A.; Peng, C. Y.; Nanayakkara, A.; Challacombe, M.; Gill, P. M. W.; Johnson, B.; Chen, W.; Wong, M. W.; Gonzalez, C.; Pople, J. A. *Gaussian 03, Revision E.01*; Gaussian, Inc.: Wallingford, CT, 2004.
(30) Becke, A. D. *Phys. Rev. A* **1988**, *38*, 3098–3100. Lee, C. T.; Yang, W. T.; Parr, R. G. *Phys. Rev. B* **1988**, *37*, 785–789.
(31) Cheng, H. L.; Lin, W. Q.; Wu, F. C. *Appl. Phys. Lett.* **2009**, *94*, 223302.
(32) In order to determine the microcrystalline structure of the rr-P3HT films onto the SiO_2 dielectric with the same surface conditions, the film for X-ray diffraction (XRD) measurements was deposited onto the oxygen plasma-treated SiO_2/glass substrate without ITO electrodes, because we could not observe a well-resolved XRD spectrum of the rr-P3HT films which in the small active channel of TFT device.
(33) To minimize the influence from measuring environments, e.g., moisture, oxygen, and light, all the long-term electrical measurements were performed in the N_2 filled glovebox in the dark. Therefore, only the spectra of the rr-P3HT films in the initial and in the final states were measured.
(34) Kobashi, M.; Takeuchi, H. *Macromolecules* **1998**, *31*, 7273–7278.
(35) Brown, P. J.; Thomas, D. S.; Köhler, A.; Wilson, J. S.; Kim, J.-S.; Ramsdale, C. M.; Sirringhaus, H.; Friend, R. H. *Phys. Rev. B* **2003**, *67*, 064203.
(36) Cornil, J.; Dos Santos, D. A.; Crispin, X.; Silbey, R.; Brédas, J.-L. *J. Am. Chem. Soc.* **1998**, *120*, 1289–1299. Manas, E. S.; Spano, F. C. *J. Chem. Phys.* **1998**, *109*, 8087–8101. Beljonne, D.; Cornil, J.; Silbey, R.; Millié, P.; Brédas, J.-L. *J. Chem. Phys.* **2000**, *112*, 4749–4758.
(37) Gierschner, J.; Huang, Y. S.; Averbeke, B. V.; Cornil, J.; Friend, R. H.; Beijonne, D. *J. Chem. Phys.* **2009**, *130*, 044105.
(38) Barford, W. *J. Chem. Phys.* **2007**, *126*, 134905.
(39) For examples, see: (a) Su, L. T.; Chung, J. E.; Antoniadis, D.; Goodson, K. E.; Flik, M. I. *IEEE Trans. Electron Devices* **1994**, *41*, 69–75. (b) Wang, L.; Fjeldly, T. A.; Iniguez, B.; Slade, H. C.; Shur, M. *IEEE Trans. Electron Devices* **2000**, *47*, 387–397. (c) Inoue, S.; Ohshima, H.; Shimoda, T. *Jpn. J. Appl. Phys.* **2002**, *41*, 6313–6319.
(40) Chabinyc, M. L.; Lu, J.-P.; Street, R. A.; Wu, Y.; Liu, P.; Ong, B. S. *J. Appl. Phys.* **2004**, *96*, 2063–2070.
(41) Louarn, G.; Trznadel, M.; Buisson, J. P.; Laska, J.; Pron, A.; Lapkowski, M.; Lefrant, S. *J. Phys. Chem.* **1996**, *100*, 12532–12539.
(42) (a) Sakamoto, A.; Furukawa, Y.; Tasumi, M. *J. Phys. Chem.* **1992**, *96*, 1490–1494. (b) Cheng, H. L.; Lin, K. F. *J. Polym. Res.* **1999**, *6*, 123–131.
(43) Using a 532 nm laser: for the initial films, the standard deviation of peak center, β, and peak intensity (integrated peak area) of the v_1 band are within 0.05 cm^{-1}, 0.4 cm^{-1}, and 6% (6%); for the annealed films, the corresponding values are within 0.2 cm^{-1}, 0.7 cm^{-1}, and 6% (7%). Using a 633 nm laser: for the initial films, the standard deviation of peak center, β, and peak intensity (integrated peak area) of the v_1 band are within 0.1 cm^{-1}, 0.2 cm^{-1}, and 8% (13%); for the annealed films, the corresponding values are within 0.06 cm^{-1}, 0.2 cm^{-1}, and 7% (8%).
(44) (a) Barbara, P. F.; Meyer, T. J.; Ratner, M. A. *J. Phys. Chem.* **1996**, *100*, 13148–13168. (b) Myers, A. B. *Chem. Rev.* **1996**, *96*, 911–926. (c) Cheng, H. L.; Liang, X. W.; Chou, W. Y.; Mai, Y. S.; Yang, C. Y.; Chang, L. R.; Tang, F. C. *Org. Electron.* **2009**, *10*, 289–298.
(45) (a) Gotlib, Y. Y.; Lyulin, S. V. *Macromol. Theory Simul.* **1996**, *5*, 449–465. (b) Chen, C.-L.; Hua, C.-Y.; Wu, C.-R. *Macromol. Theory Simul.* **2001**, *10*, 644–650.
(46) Sugita, A.; Tadaka, S. *J. Polym. Sci., Part B: Polym. Phys.* **2004**, *42*, 4433–4439.
(47) Kakade, M. V.; Givens, S.; Gardner, K.; Lee, K. H.; Chase, D. B.; Rabolt, J. F. *J. Am. Chem. Soc.* **2007**, *129*, 2777–2782.
(48) Joshi, S.; Pingel, P.; Grigorian, S.; Panzner, T.; Pietsch, U.; Neher, D.; Forster, M.; Scherf, U. *Macromolecules* **2009**, *42*, 4651–4660.